# Fatigue Strength of Amorphous Alloy Wires

# Fatigue Strength of Amorphous Alloy Wires*

Akihisa Inoue, Michiaki Hagiwara** and Tsuyoshi Masumoto

Institute for Materials Research
( Received January 25, 1988 )

## Synopsis

Amorphous alloy wires in iron-, cobalt- and nickel-based alloy systems have recently attracted strong attention as a new type of engineering materials because of high mechanical strength, good ductility, good corrosive resistance and unique magnetic properties as well as fine geometry with circular cross section. This review aims to present the fundamental characteristics of fatigue strength of iron-, cobalt- and nickel-based amorphous wires by focussing on the following points; (1) the difference in fatigue strength among iron-, cobalt- and nickel-based amorphous wires, (2) the difference in fatigue strength between repetitive bending and tensile loads, (3) the mechanism of the initiation and propagation of fatigue crack, and (4) the influences of stress ratio, testing temperature, cold drawing, structural relaxation and environment on the fatigue strength and fracture morphology. Additionally, the advantage and disadvantage to use the amorphous wire as a reinforcing material for rubber tire have briefly been discussed based on the fundamental characteristics of fatigue strength.

## I. Introduction

An amorphous alloy has been known[1,2] to exhibit high mechanical strengths combined with high fracture toughness and good ductility, in marked contrast to an extremely brittle nature of the other amorphous materials such as semiconductor and insulator. In order to make the

---

* The 1830th report of Institute for Materials Research.
** Unitika Research and Development Center, Unitika Ltd., Uji 611, Japan.

best use of the attractive mechanical properties of amorphous alloys, the fabrication of an amorphous alloy wire with a circular cross section has strongly been desired since the discovery[1] of high strength and good ductility for amorphous alloys. In 1980, we have suceeded for the first time in producing palladium-[3], iron-[4,5] and cobalt-[6] based amorphous wires by melt spinning in rotating water in a collaborate research between Tohoku University and Unitika Ltd. Furthermore, the iron- and cobalt-based amorphous wires have been found to exhibit high values of tensile fracture strength[4-6], bend ductility[4-6] and fatigue strength[7] as well as unique soft ferromagnetism[8-10] different from that of ribbon-shaped amorphous alloys, in addition to good cold-[4-6] and warm-drawability[11]. Very recently, Unitika Ltd. has developed established equipments and techniques to mass-produce iron-, cobalt- and nickel-based amorphous wires with a length as long as several kilometers[12]. Owing to the good mechanical and ferromagnetic properties of the amorphous alloy wires and the energy- and labor-saving process of producing amorphous alloy wires with a fine diameter of 80 to 200 μm directly from melt, amorphous alloy wires have attracted great interest as a new type of engineering material. This paper aims to review the fundamental characteristics of static and dynamic mechanical strengths of iron-, cobalt- and nickel-[13] based amorphous wires.

## II. Fabrication Method and Alloy Systems of Amorphous Alloy Wires

The following seven methods have been usually known as the techniques of producing wire-shaped samples directly from melts; (1) melt extrusion[14-16], (2) chill-block melt spinning[14,17,18], (3) pendant drop melt extraction[14,18], (4) melt drag[14], (5) crucible melt extraction[19,20], (6) glass-coated melt spinning[21], and (7) in-rotating-liquid spinning[22]. Among these techniques, the technique, in which iron- and cobalt-based amorphous wires with a circular cross section can be produced, has been limited to the glass-coated melt spinning[23,24] and the in-rotating-water spinning[4-6]. However, the glass-coated spinning technique has some serious disadvantages; (1) a wire diameter is usually limited to below about 10 μm, (2) melting temperature of alloys has the same level as the softening temperature of coated glass, and (3) the coated glass must be eliminated. The in-rotating-water spinning technique is thought to be the most favorable method to produce long amorphous alloy wires with diameters ranging from 80 to 200 μm. Figure 1 shows a schematic illustration of the in-

rotating-water spinning equipment which can produce an amorphous wire. The details of the spinning condition have been presented in some previous references[4-6,25].

Here it is very important to note that the formation of an amorphous alloy wire by this technique is limited to the fllowing alloy systems because of a limited glass-forming capacity of molten alloys; Fe-Si-B[4], Fe-M-Si-B (M=transition metal)[4], Fe-P-C[5], Fe-M-P-C[5], Co-Si-B[6], Co-M-Si-B[6], Ni-Si-B-Al[13], Ni-M-Si-B-Al[13], Ni-P-B-Al[13], Ni-M-P-B-Al[13], Ni-Pd-P[25], Pd-Si[26], Pd-M-Si[3] and Cu-Zr[27]. Since the wire diameter produced by the in-rotating-water spinning technique is usually in the range from 80 to 200 μm, one must choose an alloy composition at which an amorphous single phase can be formed even for the wire with diameters larger than about 80 μm. Thus, the limitation of alloy systems where an amorphous alloy wire is obtained results mainly from the glass-forming capacity, in addition to another factor that viscosity of molten alloys is high enough to keep good stability of the melt jet even in rotating water. Furthermore, it is a matter of course to adjust appropriately the spinning conditions of ejecting temperature of molten alloy, water temperature and the ratio of jet velocity of molten alloy to water velocity etc. As an example, Fig. 2 shows the glass-forming capacity of Fe-Si-B alloys[28] which have great importance from an engineering point of view. The numbers in the figure represent the maximum sample thickness for the formation of an amorphous single phase. This figure indicates a possibility that the amorphous wire is formed at the compositions with the critical thickness above about 80 μm. It is thus very important for the production of an amorphous wire to know the glass-forming capacity of each alloy. A similar compositional dependence of the glass-forming capacity has been clarified for engineeringly important Fe-P-C[28], Co-Si-B[28], Ni-Si-B[29] and Ni-P-B[13] alloys.

## III. Thermal Stability

Since an amorphous structure is in a non-equilibrium state, it is very important to note the thermal stability of amorphous alloy wires such as glass transition temperature ($T_g$), crystallization temperature ($T_x$), heat of crystallization ($\Delta H_x$) and the ratio of annealing temperature($T_f$), at which the wire annealed for 3.6 ks begins to fracture during a 180 degree bending deformation, to $T_x$ ($T_f/T_x$). Table 1 summarizes typical alloy compositions, maximum wire diameter ($D_{max}$), $T_g$, $T_x$, $\Delta H_x$ and $T_f/T_x$. The alloy systems of amorphous alloy wires

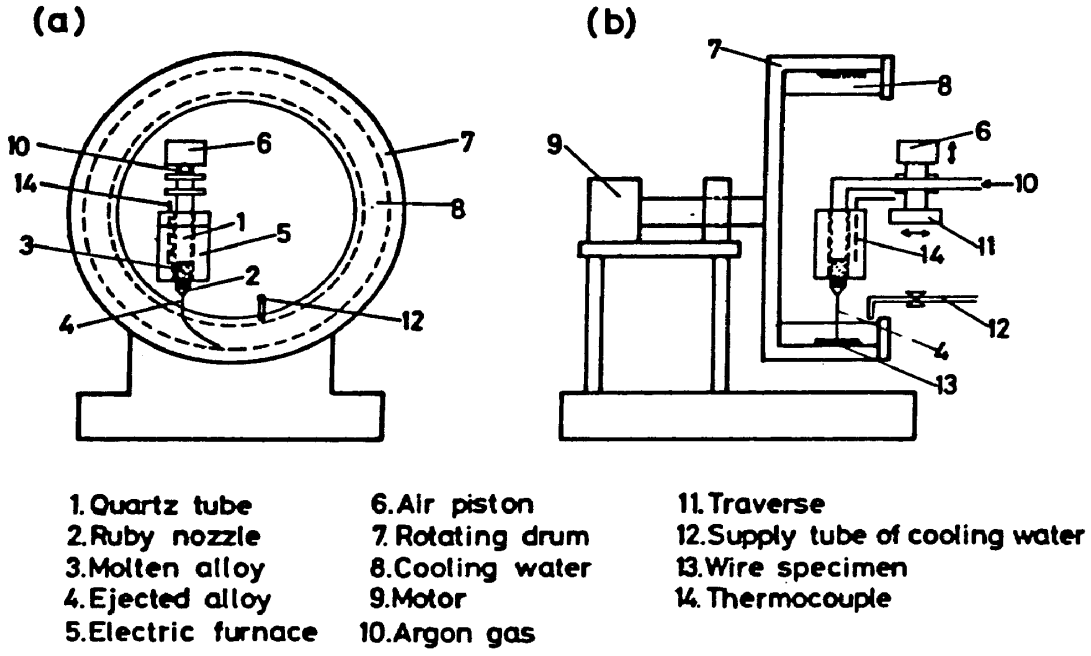


Fig. 1 Schematic illustrations of the melt-quenching apparatus for the production of amorphous wires.
(a) frontal view, (b) side view.

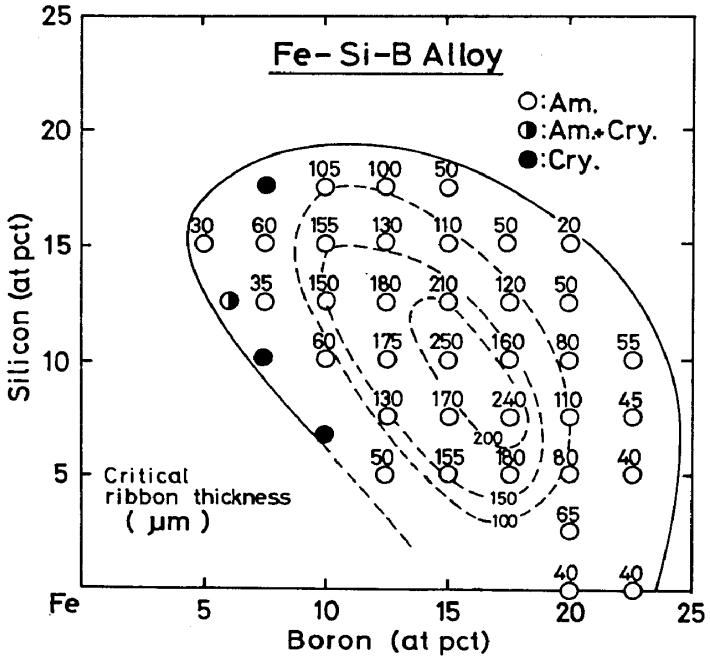


Fig. 2 Composition range and the critical ribbon thickness for the formation of an amorphous single phase in Fe-Si-B ternary alloys.

Table 1 Maximum wire diameter ($D_{max}$) and thermal stability of Fe-, Co-, Ni-, Pd- and Cu-based amorphous wires; glass transition temperature ($T_g$), crystallization temperature ($T_x$), heat of crystallization ($\Delta H_x$) and the ratio of annealing temperature, at which the wire annealed for 3.6 ks begins to fracture during a 180 degree bending deformation, to $T_x$ upon annealing for 3.6 ks ($T_f/T_x$).

| Alloy (at%) | $D_{max}$ (μm) | $T_g$ (K) | $T_x$, 40K/min (K) | $\Delta H_x$ (kJ/mol) | $T_f/T_x$ |
|---|---|---|---|---|---|
| $Fe_{75}Si_{10}B_{15}$ | 270 | - | 805 | 8.52 | 0.79 |
| $Fe_{77.5}P_{12.5}C_{10}$ | 230 | 667 | 692 | 5.27 | 0.82 |
| $Co_{72.5}Si_{12.5}B_{15}$ | 140 | - | 800 | 4.40 | 0.95 |
| $(Ni_{.75}Si_{.08}B_{.17})_{99}Al_1$ | 200 | 745 | 755 | 3.14 | 1.06 |
| $(Ni_{.78}P_{.12}B_{.1})_{99}Al_1$ | 200 | 662 | 683 | - | 1.04 |
| $Ni_{64}Pd_{16}P_{20}$ | 270 | 583 | 642 | 3.28 | 1.0 |
| $Pd_{48}Ni_{32}P_{20}$ | 270 | 587 | 645 | 3.59 | 1.0 |
| $Pd_{77.5}Cu_6Si_{16.5}$ | 270 | 623 | 680 | 3.43 | 1.0 |
| $Cu_{60}Zr_{40}$ | 150 | 740 | 754 | 3.54 | 1.0 |

produced up to date are limited to iron-, cobalt-, nickel- and palladium-metalloids (boron, phosphorus, silicon, carbon) and metal-metal type Cu-Zr alloys and their diameters are below about 270 μm for the iron- and palladium-based alloys, 200 μm for the nickel-based alloys, 150 μm for the cobalt-based and Cu-Zr alloys. It was described in section 2 that the limitation originated from the glass-forming capacity of their molten alloys. $T_x$ and $T_g$ rise in the order of Pd-Ni-P < Pd-Cu-Si < Ni-P-B < Fe-P-C < Cu-Zr ≃ Ni-Si-B < Co-Si-B ≃ Fe-Si-B and hence the amorphous alloy wires with high stability against crystallization are obtained in Fe-Si-B and Co-Si-B systems. However, great attention must be paid to the result that the iron-based amorphous wires become brittle upon annealing at temperatures lower by about 20 % than $T_x$. On the other hand, the nickel-, palladium- and copper-based amorphous wires have a good bend ductility even in an annealing-induced duplex structure of amorphous plus nickel, palladium or copper just before the appearance of crystalline compounds.

## IV. Static Mechanical Strengths

Young's modulus (E), tensile fracture strength ($\sigma_f$), Vickers hardness ($H_v$), tensile fracture strain ($\varepsilon_f$), tensile yield strain ($\varepsilon_y=H_v/3E$) of Fe-Si-B, Fe-P-C, Co-Si-B, Ni-Si-B-Al, Pd-Cu-Si, Pd-Ni-P, Pt-Ni-P and Cu-Zr amorphous wires are listed in Table 2[30], where the data of density (ρ) and sound velocity ($V_E$) are also shown for reference. The approximation of $\varepsilon_y=H_v/3E$ is based on the fact that amorphous alloys exhibit little work-hardening and thus the tensile fracture-strength is related by $\sigma_f=1/3\ H_v$[31]. With increasing metalloid content, all the amorphous alloy wires exhibit appreciable increases of E, $\sigma_f$ and $H_v$, e.g., E, $\sigma_f$ and $H_v$ of Fe-Si-B wires increase from $15.8\times10^4$ to $18.7\times10^4$ MPa, 2910 to 3920 MPa and 830 to 1100 DPN, respectively, which are much higher than those of commercial piano wires with the highest strength in conventional crystalline alloys. The highest values of E, $\sigma_f$ and $H_v$ in each alloy system decrease in the order of Fe-Si-B > Co-Si-B > Fe-P-C > Ni-Si-B > Ni-P-B > Pd-Ni-P > Pt-Ni-P > Pd-Cu-Si > Cu-Zr. The high values of E, $\sigma_f$ and $H_v$ for Fe-Si-B and Co-Si-B amorphous wires have been clarified[4,6] to increase further by the replacement of iron or cobalt by transition metals of niobium, tantalum, chromium, molybdenum, tungsten etc., as shown in Fig. 3 (a) and (b).

It is expected that E, which reflects the ease of internal dis-

Table 2 Young's modulus(E), tensile fracture strength($\sigma_f$), Vickers hardness($H_V$), tensile fracture strain($\varepsilon_f$), yield strain($\varepsilon_y$), density($\rho$) and sound velocity($V_E$) for Fe-, Co-, Ni-, Pd-, Pt- and Cu-based amorphous wires.

| Alloy (at%) | E(MPa) | $\sigma_f$(MPa) | $H_V$ (DPN) | $\varepsilon_f$ (%) | $\varepsilon_y = H_V/3E$(%) | $\rho$ (Mg/m$^3$) | $V_E$ (km/s) |
|---|---|---|---|---|---|---|---|
| $Fe_{80}Si_{10}B_{10}$ | 158000 | 2910 | 830 | 2.1 | 1.7 | 7.27 | 4.655 |
| $Fe_{77.5}Si_{10}B_{12.5}$ | 164000 | 3100 | 935 | 2.4 | 1.9 | 7.21 | 4.773 |
| $Fe_{75}Si_{10}B_{15}$ | 171000 | 3410 | 1030 | 2.8 | 2.0 | 7.16 | 4.884 |
| $Fe_{70}Si_{10}B_{20}$ | 187000 | 3920 | 1100 | 2.3 | 1.9 | 7.05 | 5.156 |
| $Fe_{80}P_{12.5}C_{7.5}$ | 140000 | 2730 | 810 | 2.6 | 1.9 | 7.27 | 4.410 |
| $Fe_{77.5}P_{12.5}C_{10}$ | 141000 | 2790 | 815 | 2.7 | 1.9 | 7.25 | 4.404 |
| $Fe_{75}P_{15}C_{10}$ | 144000 | 2820 | 810 | 2.6 | 1.8 | 7.23 | 4.470 |
| $Fe_{75}P_{10}C_{15}$ | 152000 | 2990 | 895 | 2.8 | 1.9 | 7.28 | 4.558 |
| $Co_{77.5}Si_{12.5}B_{10}$ | 190000 | 3580 | 1140 | 3.0 | 2.1 | 7.72 | 4.731 |
| $Co_{75}Si_{10}B_{15}$ | 174000 | 3180 | 1070 | 2.5 | 2.0 | 7.85 | 4.714 |
| $Co_{72.5}Si_{12.5}B_{15}$ | 174000 | 3450 | 1130 | 3.0 | 2.1 | 7.74 | 4.731 |
| $Co_{70}Si_{15}B_{15}$ | 175000 | 3020 | 1170 | 2.6 | 2.2 | 7.60 | 4.792 |
| $(Ni_{.75}Si_{.08}B_{.17})_{99}Al_1$ | 151000 | 2730 | 780 | 2.9 | 1.7 | - | - |
| $(Ni_{.78}P_{.12}B_{.10})_{99}Al_1$ | 125000 | 2170 | 690 | 2.4 | 1.8 | - | - |
| $Pd_{77.5}Cu_6Si_{16.5}$ | 87800 | 1560 | 390 | 2.3 | 1.4 | 10.3 | 2.918 |
| $Pd_{48}Ni_{32}P_{20}$ | 95700 | - | 470 | - | 1.6 | 10.07 | 3.099 |
| $Pt_{60}Ni_{15}P_{25}$ | 93500 | - | 385 | - | 1.3 | 15.71 | 2.439 |
| $Cu_{65}Zr_{35}$ | - | 1670 | 425 | 2.4 | - | - | - |
| $Cu_{60}Zr_{40}$ | - | 1810 | 440 | 2.7 | - | - | - |

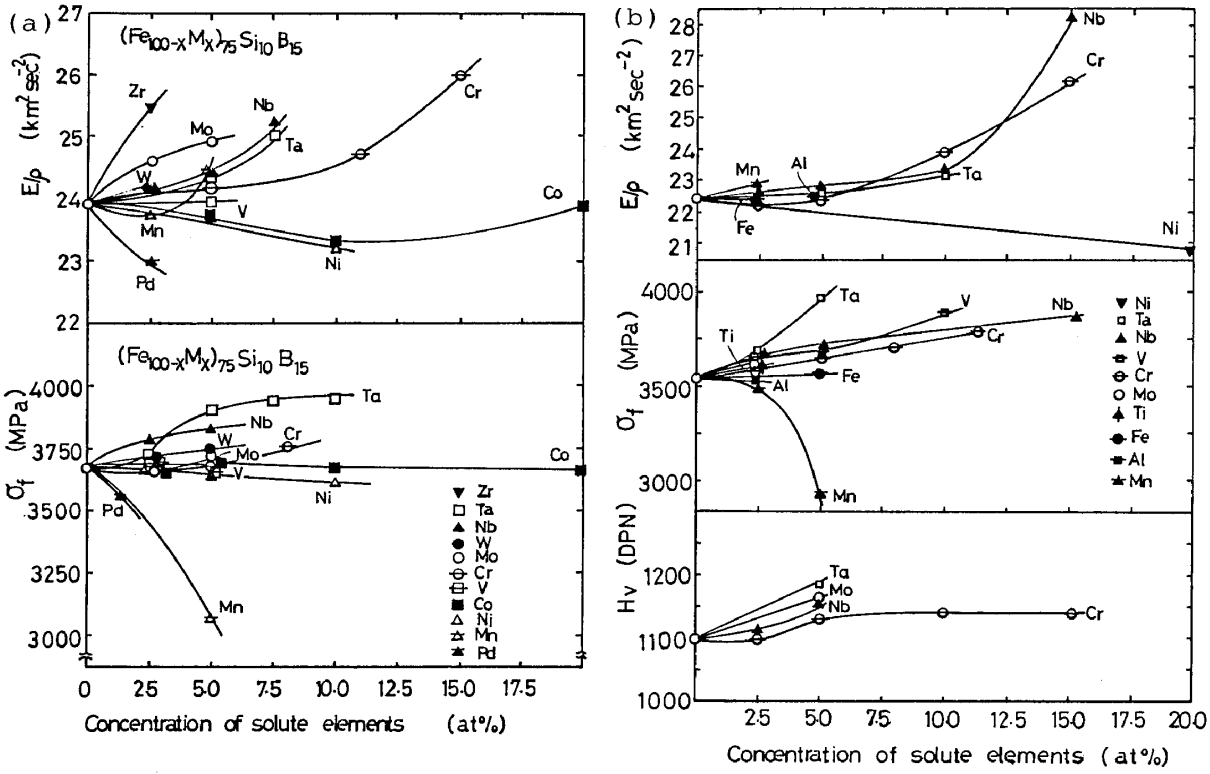


Fig. 3 Changes in the Young's modulus (E), tensile fracture strength ($\sigma_f$) and Vickers hardness ($H_V$) of $(Fe_{100-x}M_x)_{75}Si_{10}B_{15}$ (a) and $(Co_{100-x}M_x)_{72.5}Si_{12.5}B_{15}$ (b) amorphous wires with solute element content (M=V, Nb, Ta, Cr, Mo, W, Mn, Fe, Co, Ni or Pd).

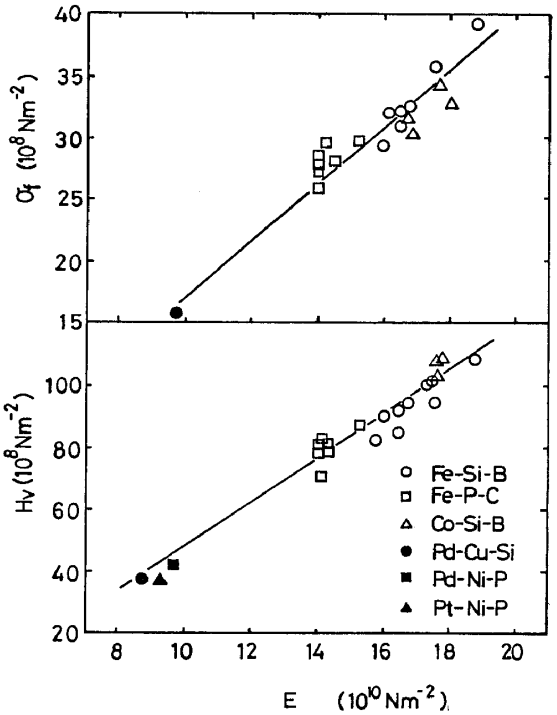


Fig. 4 The correlation between Young's modulus (E) and tensile fracture strength ($\sigma_f$) or Vickers hardness ($H_V$) for Fe-Si-B, Fe-P-C, Co-Si-B, Pd-Cu-Si, Pd-Ni-P and Pt-Ni-P amorphous wires.

placement, strongly correlates to $\sigma_f$ and $H_v$. Figure 4 shows the changes in $\sigma_f$ and $H_v$ as a function of E for iron-, cobalt-, palladium- and platinum-based amorphous wires. The data points are located in a scatter band following a roughly linear relationship. It is noteworthy in Table 2 and Fig. 4 that the observed ratio of $\sigma_f$ to E shows an almost constant value of about 0.020 for all amorphous wires investigated, in spite of significant differences in $\sigma_f$ as well as E. The observed ratio of E to $\sigma_f$ is much larger than that (0.01 to 0.005) of conventional steels and may be comparable to that ($\simeq$0.06) of iron whiskers[32]. The result allows us to state the following two common features on the static mechanical properties of amorphous alloy wires: (a) increasing $\sigma_f$ is associated with an increasing stiffness and the mechanism of such changes is the same between E and $\sigma_f$, and (b) there is no evident change in the plastic flow mechanism for all of the amrorhous wires. Accordingly it may be concluded that the variations in E, $\sigma_f$ and $H_v$ with alloy composition are not due to the difference in flow mechanism but attributed to the change in the short-range ordering.

The effect of the replacement of iron or cobalt by transition M metals on the E, $\sigma_f$ and $H_v$ values of iron- and cobalt-based amorphous wires shown in Fig. 3 has been interpreted[30] by taking the average group number (AGN) of metallic atoms in amorphous alloys into consideration. Figure 5 shows the Young's modulus sound velocity ($V^2=E/\rho$) of $(Fe\text{-}M)_{75}Si_{10}B_{15}$ and $(Co\text{-}M)_{72.5}Si_{12.5}B_{15}$ amorphous wires as a function of AGN. From the strong dependence of $E/\rho$ on AGN, the large changes of E, $\sigma_f$ and $H_v$ of the iron- and cobalt-based amorphous wires are presumably due to structural and compositional orderings through the strong interaction between metal and metalloid atoms.

The strain rate dependence of $\sigma_f$ for $Fe_{75}Si_{10}B_{15}$ amorphous wire has been examined and $\sigma_f$ has been clarified[33] to decrease almost linearly with increasing strain rate, i.e., from 3280 MPa at $1.6\times10^{-5}$ $s^{-1}$ to 3200 MPa at $3.4\times10^{-3}$ $s^{-1}$. This dependence is in marked contrast to the general tendency for crystalline iron-based alloys. The contrast behavior for an amorphous alloy is thought as due to the decrease in fracture stress caused by an adiabatic temperature rise at an inhomogeneous deformation site with increasing strain rate. No distinct change in the fracture appearance consisting of vein and smooth regions with strain rate is seen for the Fe-Si-B amorphous wire.

The temperature dependence of $\sigma_f$ is shown in Fig. 6 for $Fe_{75}Si_{10}B_{15}$ amorphous wire. As the testing temperature rises from 292 to 527 K, $\sigma_f$ decreases almost linearly from 3230 MPa to 2710 MPa. A

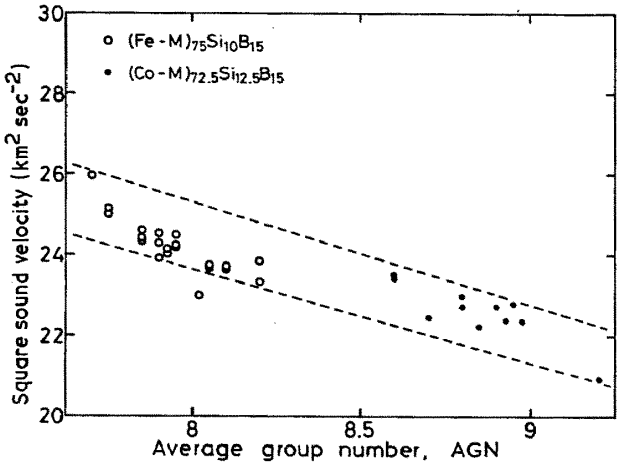


Fig. 5 Change in the square sound velocity $V^2=E/\rho$ of $(Fe-M)_{75}Si_{10}B_{15}$ and $(Co-M)_{72.5}Si_{12.5}B_{15}$ amorphous wires with the average group number of metallic atom (AGN), M=Zr, V, Nb, Ta, Cr, Mo, W, Mn, Fe, Co, Ni or Pd.

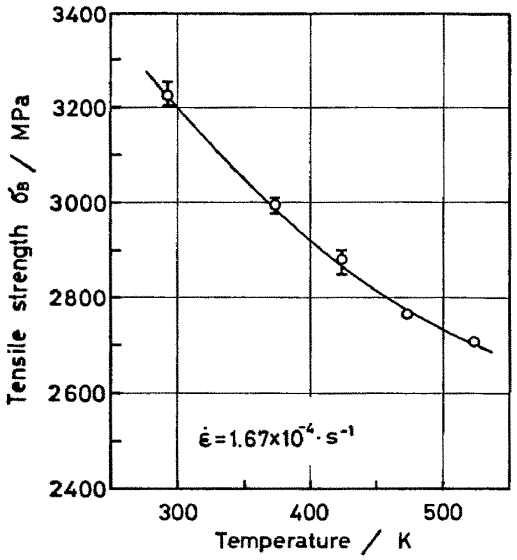


Fig. 6 Change in tensile fracture strength of $Fe_{75}Si_{10}B_{15}$ amorphous wire as a function of testing temperature.

Table 3 Comparison of Young's modulus (E) and structural relaxation enthalpy ($\Delta H_{relax}$) in the wire and ribbon samples for $Fe_{75}Si_{10}B_{15}$, $Fe_{77.5}P_{12.5}C_{10}$, $Co_{72.5}Si_{12.5}B_{15}$, $(Ni_{.75}Si_{.08}B_{.17})_{99}Al_1$ and $(Ni_{.78}P_{.12}B_{.1})_{99}Al_1$ amorphous wires.

| Alloy (at%) | Diameter or Thickness(μm) | E (MPa) | Ratio of change(%) | $\Delta H_{relax}$ (J/mol) | Ratio of change(%) |
|---|---|---|---|---|---|
| $Fe_{75}Si_{10}B_{15}$ | | | | (T≤730K) | |
| wire | 120 | 171000 | +3.4 | 615 | -2.6 |
| ribbon | 20 | 177000 | | 599 | |
| $Fe_{77.5}P_{12.5}C_{10}$ | | | | (T≤690K) | |
| wire | 110 | 141000 | +0.7 | 907 | -4.7 |
| ribbon | 20 | 142000 | | 864 | |
| $Co_{72.5}Si_{12.5}B_{15}$ | | | | (T≤730K) | |
| wire | 100 | 174000 | +1.1 | 720 | -2.7 |
| ribbon | 23 | 176000 | | 523 | |
| $(Ni_{.75}Si_{.08}B_{.17})_{99}Al_1$ | | | | (T≤720K) | |
| wire | 120 | 151000 | +1.3 | 237 | -11.8 |
| ribbon | 40 | 153000 | | 209 | |
| $(Ni_{.78}P_{.12}B_{.1})_{99}Al_1$ | | | | (T≤650K) | |
| wire | 115 | 125000 | +1.6 | 235 | -5.1 |
| ribbon | 40 | 127000 | | 223 | |

similar temperature dependence has been recognized[34] for the other cobalt- and nickel-based amorphous wires. The significant decrease in $\sigma_f$ with rising temperature is probably because viscous flow at a highly stress-concentrated deformation site becomes easy through the increase in mobility of the constituent atoms.

## V. Features of Young's Modulus and Structural Relaxation Behavior of Amorphous Alloy Wires in Comparison with Amorphous Alloy Ribbons

Table 3 summarizes E and structural relaxation enthalpy ($\Delta H_{relax}$) in the wire and ribbon forms for $Fe_{75}Si_{10}B_{15}$, $Fe_{77.5}P_{12.5}C_{10}$, $Co_{72.5}Si_{12.5}B_{15}$, $(Ni_{0.75}Si_{0.08}B_{0.17})_{99}Al_1$ and $(Ni_{0.78}P_{0.12}B_{0.1})_{99}Al_1$ alloys, along with the data of wire diameter and ribbon thickness[13,30,35]. It is rather striking that E and $\Delta H_{relax}$ of their amorphous wires are smaller by about 0.7 to 3.4 % and larger by about 2.6 to 2.7 %, respectively, than those of the amorphous ribbons, since it has generally been recognized that E increases with structural relaxation caused by annealing at temperatures well lower than $T_x$[36] and with increasing ribbon thickness[37] or wire diameter[38]. That is, there is a clear tendency that the larger the degree of the structural disorder the smaller is the E and the larger is the $\Delta H_{relax}$. Accordingly, it may be concluded that the wire samples (≃100 μm diameter) of Fe-Si-B, Fe-P-C, Co-Si-B, Ni-Si-B-Al and Ni-P-B-Al alloys have a more disordered structure compared with the ribbon samples (≃25 μm thickness).

It has been reported that the maximum ribbon thickness for the formation of an amorphous phase by the conventional single roller quenching technique is usually less than about 40 μm[39], whereas the maximum wire diameter for the formation of an amorphous phase by the in-rotating-water spinning method is about 270 μm for $Fe_{75}Si_{10}B_{15}$[28], about 230 μm for $Fe_{77.5}P_{12.5}C_{10}$[28], about 140 μm for $Co_{72.5}Si_{12.5}B_{15}$[28] and about 200 μm for $(Ni_{0.75}Si_{0.08}B_{0.17})_{99}Al_1$[13]. Therefore, it appears that the wire samples exhibited lower E and larger $\Delta H_{relax}$ compared with the ribbon samples due to the much larger glass-forming capacity for the in-rotating-water spinning method. The large discrepancy is considered to originate from the inherent differences in the solidfication process of the ejected melt as well as in the method of cooling after solidification: That is, in the case of the single roller quenching method, the solidification of the melt is achieved only through contact with the roller[40] with contact time and length

as short as about 0.01 s and 100 mm[41], respectively, for Fe-Si-B alloys. The solidified ribbon detaches itself from the roller at or above the glass transition and is air-cooled to room temperature. On the other hand, in the in-rotating-water spinning method, the rapidly circulating water cools the melt continuously up to the water temperature over the entire outside surface of the wire[23,25].

## VI. Fatigue Strength under Dynamic Bending Load

### 1. Bending-type fatigue testing apparatus

The fatigue test was performed on amorphous wires with a gauge dimension of 100 mm at a frequency of 3.2 Hz at 293 K in air, where the humidity was controlled, as well as in water. Figure 7 shows a schematic illustration of specially designed bending-type fatigue testing machine consisting of three pulleys. The maximum applied strain ($\lambda$) leading to fatigue failure under condition of dynamic bending load was measured as a function of the number of cycles of strain ($N_f$). The $\lambda$ was adjusted by changing the diameter of the pulley (2r) and evaluated by the relation of $\lambda=d/(2r+d)$, where d is the wire diameter.

### 2. Fatigue strength in humid air

Typical $\lambda$-$N_f$ curves in air having the relative humidity(RH)=65 % are shown in Fig. 8 for $Fe_{75}Si_{10}B_{15}$ and $Fe_{77.5}P_{12.5}C_{10}$ amorphous wires[7] and Fig. 9 for $Co_{72.5}Si_{12.5}B_{15}$[42], $(Ni_{0.75}Si_{0.08}B_{0.17})_{99}Al_1$[13] and $(Ni_{0.78}P_{0.12}B_{0.10})_{99}Al_1$[13] amorphous wires. In Fig. 8, the data of piano wire and SUS304 (18Cr-8Ni stainless steel) wire as well as Fe-Si-B and Fe-P-C amorphous ribbons are also presented for comparison. One can see the existence of so-called "fatigue limit" defined as the highest strain at which a non-failure is observed at an arbitrary number of cycles (for example, $10^6$ cycles) for the amorphous wires and ribbons as well as for the crystalline wires. The fatigue limit is about 0.0032 for the Fe-Si-B wire, 0.0030 for the Fe-P-C wire, 0.0032 for the Co-Si-B wire, 0.0050 for the Ni-Si-B-Al wire and 0.0035 for the Ni-P-B-Al wire. Thus, the fatigue strength is highest for Ni-Si-B-Al wire, followed by Ni-P-B-Al, Fe-Si-B, Co-Si-B and then Fe-P-C wires. A similar tendency is also seen for the fatigue strength in the region of small $N_f$ values where larger bending strain was applied. Additionally, the fatigue limits of the iron-based amorphous wires are about two times as large as those (0.0017-0.0019)[43] for the iron-based amorphous ribbons but the values are lower by about

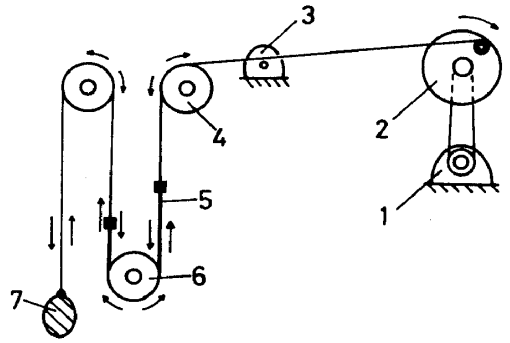


1. Motor 2. Rotating disk 3. Digital counter
4. Guide pulley 5. Sample 6. Pulley 7. Load

Fig. 7
A schematic illustration of bending-type fatigue testing machine.

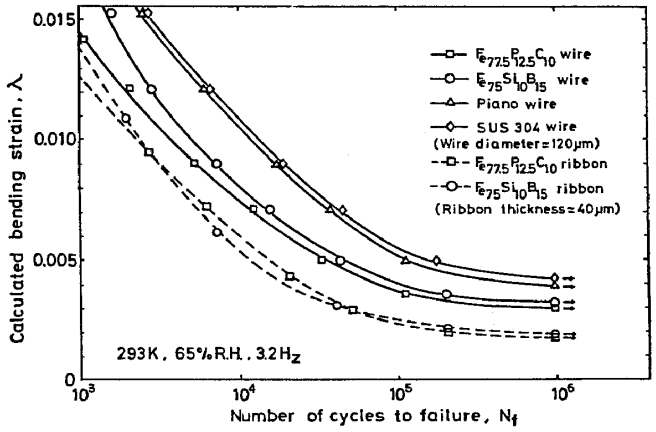


Fig. 8
Bending fatigue curves for $Fe_{75}Si_{10}B_{15}$ and $Fe_{77.5}P_{12.5}C_{10}$ amorphous wires.

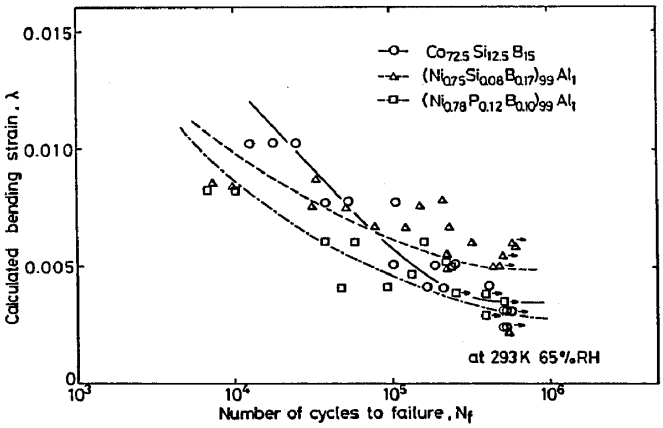


Fig. 9
Bending fatigue curves for $Co_{72.5}Si_{12.5}B_{15}$, $(Ni_{.75}Si_{.08}B_{.17})_{99}Al_1$ and $(Ni_{.78}P_{.12}B_{.10})_{99}Al_1$ amorphous wires.

35 % than those (0.0039-0.0042 %) of piano wire and SUS304 wire. In the iron-, cobalt- and nickel-based amorphous wires, it is noticed that the Ni-Si-B-Al wire exhibits fatigue strength higher than the commercial piano wire and SUS304 wire.

3. Fracture morphology

Figure 10 shows the fracture surface appearance of $Fe_{75}Si_{10}B_{15}$ wire failured at $N_f=5.4\times10^5$ under $\lambda=0.0040$ in air with RH=65 %. The photograph reveals the following three important points: (1) The fatigue crack initiates on the wire surface marked with an arrow, propagates gradually accompanied by striation pattern to the central part on the perpendicular surface against the longitudinal direction of the wire, and then very rapidly, resulting in a final failure. (2) The spacing among striation fringes is as small as about 0.7 μm and the area ratio of the striation pattern region to the whole fracture surface is about 30 %. (3) The fracture surface produced by final failure is very smooth, in strong contrast to the result for the tensile fracture surface appearance in which a developed vein pattern is observed. As the applied bending strain increases, the spacing among the striation fringes becomes coarse and the fraction of the area occupied with the striation fringe tends to decrease.

4. Improvement of fatigue strength by the reduction of humidity

Figure 11 shows the $\lambda$-$N_f$ curves of $Fe_{75}Si_{10}B_{15}$ amorphous wire tested in air having various RH values. With decreasing RH value, the fatigue limit increases significantly from 0.0025 at RH=85 % to 0.010 at RH=30 %. Furthermore, the influence of humidity on the $\lambda$-$N_f$ behavior becomes significant with increasing $N_f$, i.e., with increasing testing time required up to final failure. This result enables us to infer that the change in the fatigue strength with humidity arises from the time (diffusion)-controlled process such as the embrittlement due to the dissolution of hydrogen generated by dissociation of moisture. It is therefore thought that the improvement of fatigue strength for iron-based amorphous wires might be achieved in the alloy system exhibiting high corrosion resistance.

This inference is also supported from the result that the Ni-Si-B-Al amorphous wire with the highest fatigue strength in air with RH=65 % exhibits a corrosion resistance much better than that of Fe-Si-B amorphous wire. For instance, the ratio of corrosive weight loss by immersion to 4 h in a 1N HCL solution at 303 K to sample weight is

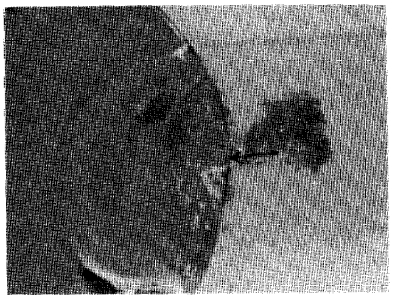

Fig. 10
Fracture surface appearance for $Fe_{75}Si_{10}B_{15}$ amorphous wire subjected to bending fatigue failure after $N_f = 5.4 \times 10^5$ under $\lambda = 0.0040$.

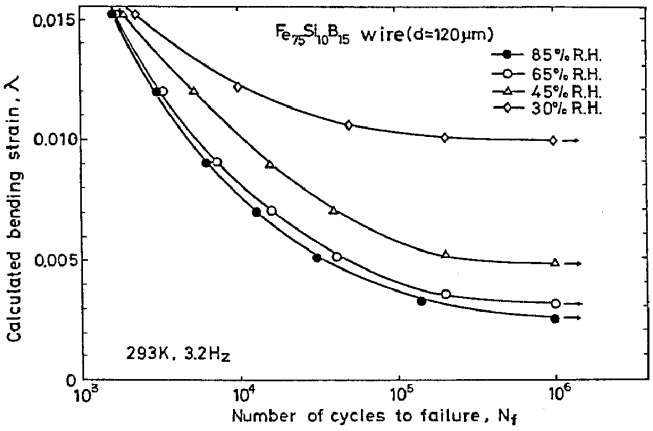


Fig. 11
Bending fatigue curves for $Fe_{75}Si_{10}B_{15}$ amorphous wires tested in air with different relative humidity.

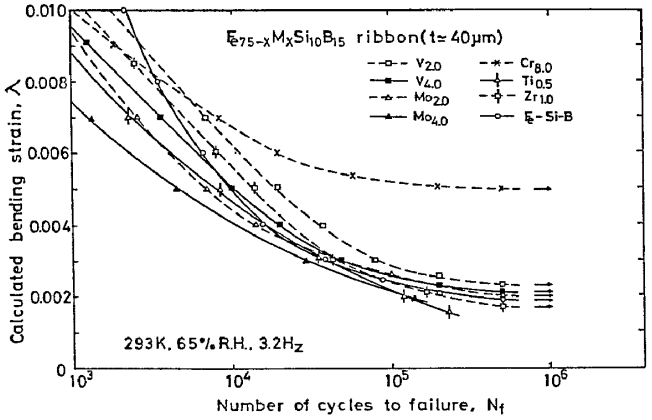


Fig. 12
Bending fatigue curves for $Fe_{75-x}M_xSi_{10}B_{15}$ (M=Ti, Zr, V, Cr or Mo) amorphous ribbons.

0.90 % for $(Ni_{0.75}Si_{0.08}B_{0.17})_{99}Al_1$ wire, 8.82 % for $(Ni_{0.78}P_{0.12}B_{0.10})_{99}Al_1$ wire and 15.86 % for $Fe_{75}Si_{10}B_{15}$ wire[13].

5. Improvement of fatigue strength by the addition of chromium

The possibility that the amorphous alloy wires with high resistance to corrosion might exhibit high fatigue stength was pointed out in subsection 6-4. The subsequent investigation was focussed on Fe-M-Si-B, Fe-M-P-C, Co-M-Si-B and Ni-M-Si-B (M=transition metal) amorphous alloys because the quaternary alloys are expected to exhibit high fatigue strength combined with good corrosion resistance. The $\lambda$-$N_f$ behavior was examined for the amorphous ribbons with a cross section of 40 m x 2 mm in $Fe_{75-x}M_xSi_{10}B_{15}$, $Fe_{77.5-x}M_xP_{12.5}C_{10}$ and $Co_{72.5-x}M_xSi_{12.5}B_{15}$ systems (M=titanium, zirconium, vanadium, niobium, tantalum, chromium, molybdenum, tungsten, manganese, iron, cobalt, nickel, palladium, copper or aluminum)[7]. As an example, Fig. 12 shows the $\lambda$-$N_f$ curves of the $Fe_{75-x}M_xSi_{10}B_{15}$ amorphous ribbons tested in air with RH=65 %. Although the fatigue limit of $Fe_{75}Si_{10}B_{15}$ ribbon is about 0.0019, the replacement of iron by 8 at% Cr gives rise to a remarkable improvement of fatigue limit to about 0.0050. The other elements have little effect on the enhancement of fatigue strength.

A similar enhancement of fatigue strength is reasonably expected to be achieved even for the amorphous wires. Figure 13 shows the fatigue limit of $Fe_{77.5-x}Cr_xP_{12.5}C_{10}$ amorphous alloys in the ribbon and wire forms as a function of chromium content. It is seen that the fatigue limit increases remarkably in the vicinity of 3 to 5 %Cr, indicating that the remarkable enhancement of fatigue limit is possible even for the amorphous wire by the dissolution of chromium more than about 5 %Cr.

The effect of chromium addition on the $\lambda$-$N_f$ curves is shown in Fig. 14 for $Fe_{75-x}Cr_xSi_{10}B_{15}$ amorphous wires and Fig. 15 for $Co_{67.5}Cr_5Si_{12.5}B_{15}$[42], $Co_{70}Cr_5Si_{15}B_{10}$[42] and $(Ni_{0.75}Si_{0.08}B_{0.17})_{93}Al_1Cr_6$[42] amorphous wires. The enhancement of the fatigue strength with increasing chromium content is seen over the entire $N_f$ region and the enhancement is as much as about 300 % for $Fe_{64}Cr_{11}Si_{10}B_{15}$ wire, about 330 % for the Co-Cr-Si-B wires and about 180 % for the Ni-Cr-Si-B-Al wire. It is very striking that the fatigue limits (0.009-0.0131) of the iron-, cobalt- and nickel-based amorphous wires containing chromium are about 2.3 to 3.3 times as high as those of commercial piano wire and SUS304 wire.

The improvement of fatigue limit by the addition of chromium was also observed for Fe-Cr-Si-B amorphous wires with different silicon

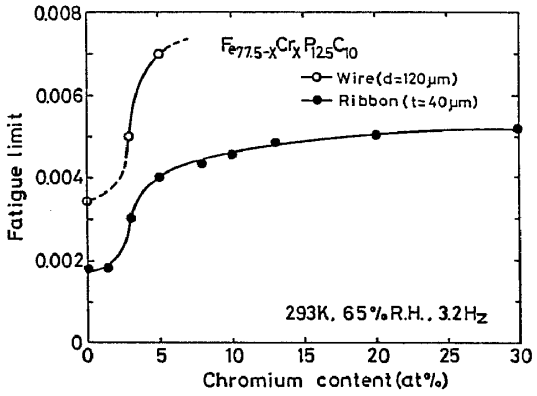


Fig. 13 Bending fatigue limit at $N_f = 10^6$ as a function of chromium content for $Fe_{77.5-x}Cr_xP_{12.5}C_{10}$ amorphous alloys in wire and ribbon forms.

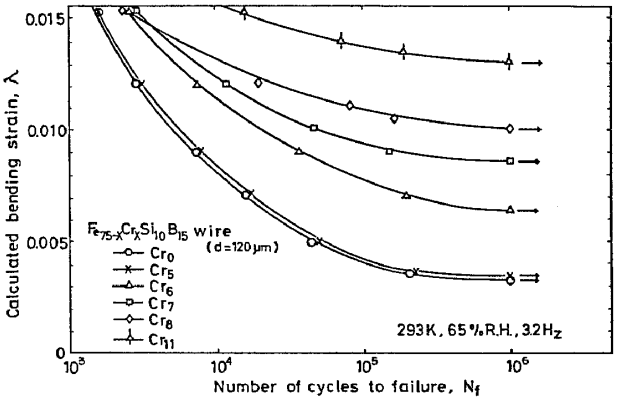


Fig. 14 Bending fatigue curves for $Fe_{75-x}Cr_xSi_{10}B_{15}$ amorphous wires.

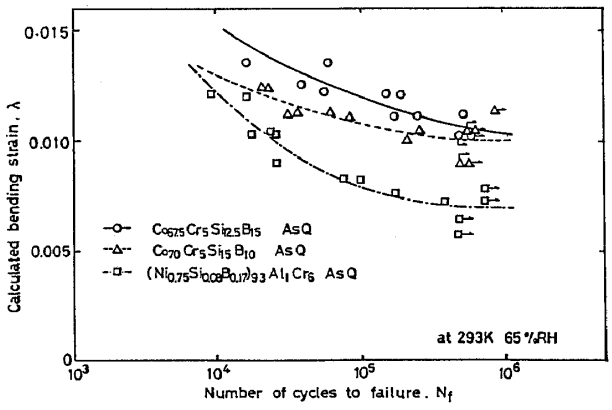


Fig. 15 Bending fatigue curves for $Co_{67.5}Cr_5Si_{12.5}B_{15}$, $Co_{70}Cr_5Si_{15}B_{10}$ and $(Ni_{.75}Si_{.08}B_{.17})_{93}Al_1Cr_6$ amorphous wires.

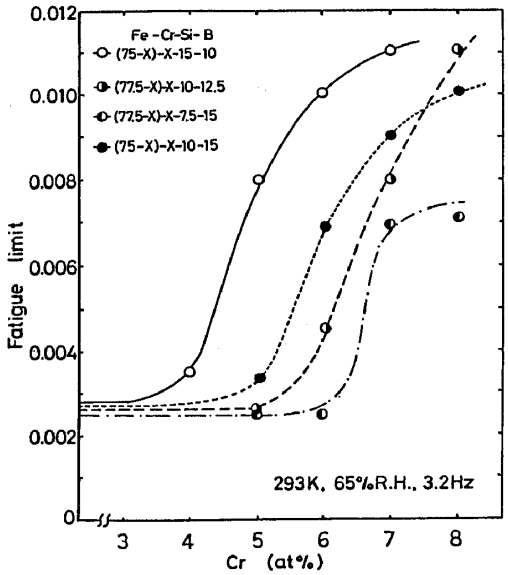


Fig. 16 Bending fatigue limit at $N_f = 10^6$ as a function of chromium content for Fe-Cr-Si-B amorphous wires with different metalloid compositions.

and boron compositions as shown in Fig. 16. The improved effect of chromium on the fatigue limit is not linear as a function of chromium content and can be divided into three stages; (a) the first stage without appreciable improvement, (b) the second stage with a rapid enhancement, and (c) the third stage where the enhancement becomes saturated. The minimum chromium content required to cause the remarkable enhancement of fatigue limit is not constant and depends strongly on metalloid composition, particularly silicon concentration; the higher the silicon concentration the larger is the effectiveness of chromium addition. Although the $Fe_{75}Si_{10}B_{15}$ alloy with the largest glass-forming capacity in Fe-Si-B ternary system has the smallest chromium concentration to enhace the fatigue limit, the reason for such a compositional tendency of the effectiveness of chromium addition remains unknown. The spontaneous formation of the passive thin film including simultaneously chromium and silicon on the outside surface of the wire appears to accelerate the improvement of fatigue strength through the enhancement of corrosion resistance.

The high fatigue strength of Fe-Cr-Si-B amorphous wires was also recognized in water. Figure 17 shows the $\lambda$-$N_f$ curves of $Fe_{75}Si_{10}B_{15}$ and $Fe_{67}Cr_8Si_{10}B_{15}$ amorphous wires tested in water at 293 K together with the data of piano wire and SUS304 wire. Although the fatigue limit decreases from 0.010 in air to 0.0075 in water even for $Fe_{67}Cr_8Si_{10}B_{15}$ wire, the fatigue strength level is about 1.9 times as high as that (0.0040) of SUS304 wire. Additionally, from the comparison of Figs. 9 and 17, the fatigue strengths in water for the piano wire and $Fe_{75}Si_{10}B_{15}$ amorphous wire without chromium decrease drastically and no fatigue limit of the two alloys is detected in water, indicating that the degradation of corrosion resistance brings about a significant reduction of fatigue strength.

It was demonstrated in the present work that the fatigue strengths of Fe-Si-B, Fe-P-C, Co-Si-B and Ni-Si-B-Al amorphous wires were remarkably enhanced by either the reduction of humidity or the addition of chromium while degraded by immersion into water. Further, it is well known that the initiation of fatigue crack ususally occurs on the sample surface. Accordingly, it is reasonably believed for the present amorphous wires that the fatigue crack under the dynamic bending force initiates on the outer surface where the largest strain is applied and propagates to the central region of the wire. The photograph shown in Fig. 10 also supports the above described inference. It may be therefore concluded that the enhancement of fatigue strength by the dissolution of chromium is due mainly to the suppression of the initiation of fatigue crack on the sample surface

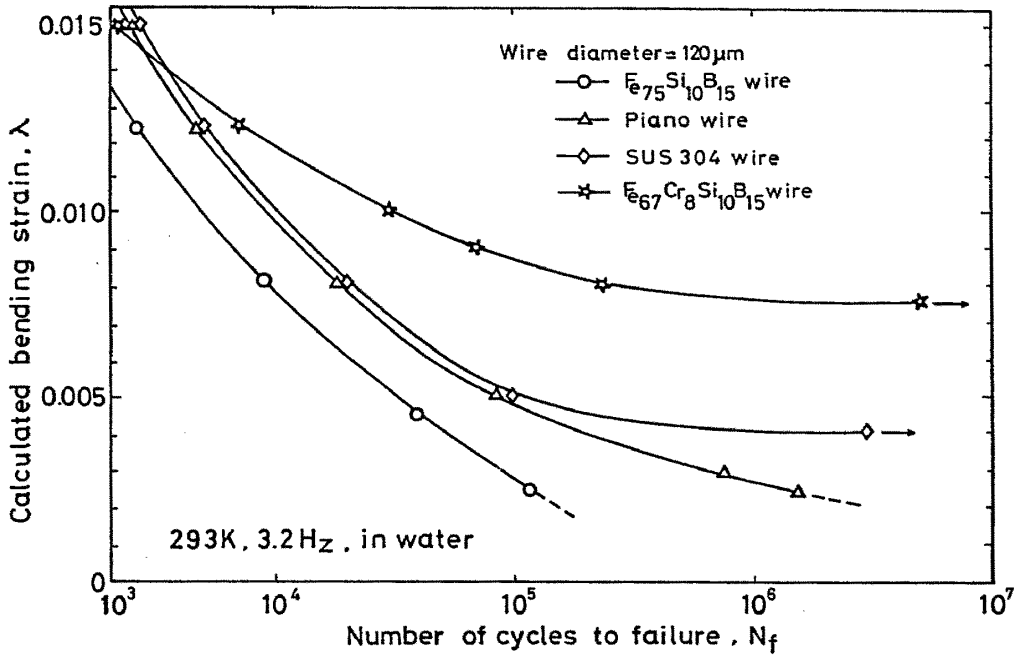


Fig. 17 Bending fatigue curves for $Fe_{75}Si_{10}B_{15}$ and $Fe_{67}Cr_8$-$Si_{10}B_{15}$ amorphous wires tested in water at 293 K.

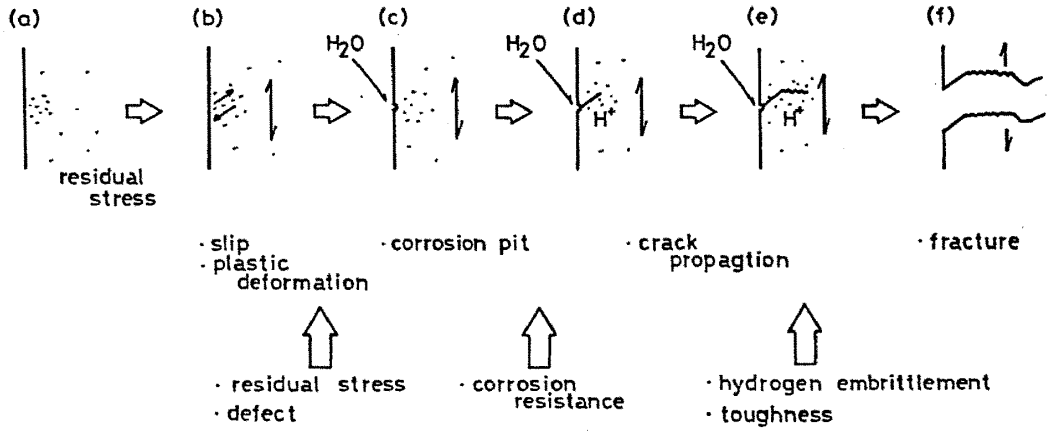


Fig. 18 Schematic illustrations showing hypothetical processes in bending fatigue failure for an amorphous alloy wire.

through the remarkable enhancement of corrosion resistance.

6. Mechanism for the initiation and propagation of fatigue crack

Figure 18 shows a hypothetical process of the initiation and propagation of fatigue crack for the amorphous alloy wires on the basis of the present results and discussion. The proceeding of the crack might take place as follows: (a) The amorphous wire usually contains a rather high residual stress. (b) The slip step due to the repetitive bending load generates in the high tensile residual stress region on the wire surface. (c) A small corrosion pit generates at the slip step in a high surface energy state. (d) The adsorption and dissociation of moisture in air become easy near the corrosion pit, resulting in the generation and dissolution of hydrogen. (e) and (f) The increases of internal stress and embrittlement sensitivity due to the dissolution of hydrogen give rise to easy initiation and propagation of fatigue crack, leading to a final fracture. It was demonstrated in subsection 6-5 that the improvement of corrosion resistance by the addition of chromium was very effective to enhance the fatigue strength of the amorphous wires. This result suggests that the suppression of the formation of the corrosion pit, where moisture is adhered and dissociated, in the initiation and propagation processes of fatigue crack is most effective to enhance the fatigue strength. Accordingly, the stage (c) in Fig. 18 is thought to be a rate-controlled process to cause the fatigue failure of the amorphous wires. The importance of this stage results from an inherent surface nature for amorphous alloys different from crystalline alloys. That is, the surface of amorphous alloys is chemically very active because of their disordered atomic configuration including a large amount of voids and/or vacancies. The easy spontaneous formation of corrosion-resistant passive film containing a large amount of chromium due to the active surface reactivity of amorphous alloys may be concluded to bring about an enhancement of fatigue strength.

At any event, the information that the fatigue strength of iron-based amorphous wires is remarkably improved by either the addition of chromium or the reduction in humidity in air gives an encouraging prospect of extensive practical use of the amorphous wires.

## VII. Fatigue Strength Under Dynamic Tensile Load

The fatigue strength of amorphous wires is expected to depend

strongly on the applied condition of stress. In this section described is the fatigue strength of $Fe_{75}Si_{10}B_{15}$ amorphous wire at different stress ratios and testing temperatures under dynamic tensile load[33]. As is presented in section 6, the $Fe_{75}Si_{10}B_{15}$ amorphous wire without chromium does not possess high fatigue strength in humid air, but the clarification of fatigue behavior under different stress conditions for the simple Fe-Si-B alloy system is very important from scientific and enginnering points of view.

1. Tensile-type fatigue testing apparatus

Figure 19 shows a schematic illustration of specially designed grips for the fatigue test under repetitive tensile load. The amorphous wires with a diameter of 125 μm were fixed by winding on the outside surface of a set of cylindrical tubes with a concave. The gauge length of the fatigue sample was 50 mm and the frequency was fixed at 30 Hz which is 9.4 times as high as that (3.2 Hz) in the bending-type fatigue test described in section 6. From the faster repetitive velocity, the fatigue limit under dynamic tensile load in this section is changed to the highest strain at which a non-failure is observed at $10^7$ cycles. The stress ratio ($R=\sigma_{min}/\sigma_{max}$) defined by the ratio of minimum applied tensile stress ($\sigma_{min}$) to maximum applied tensile stress ($\sigma_{max}$) was adjusted to be 0.2, 0.4, 0.5 and 0.6. The testing temperature was in the range from 293 to 523 K and the atmosphere was controlled in argon, hydrogen and oxygen gases with RH=20 % as well as in air with RH=20 and 65 %.

2. Fatigue strength at 293 K and its stress-ratio dependence

Figure 20 shows the $\sigma_{max}$-$N_f$ curves of $Fe_{75}Si_{10}B_{15}$ amorphous wires tested in air with RH=65 %, along with the data of commercial piano wire and high carbon steel wire. The fatigue limit of the $Fe_{75}Si_{10}B_{15}$ amorphous wire at R=0.6 is about 600 MPa, being considerably lower than those (≃1600 MPa and 1250 MPa) of piano wire and high carbon steel wire. This result agrees with the tendency under dynamic bending load. Additionally, as the stress ratio decreases, the fatigue strength of the amorphous wire decreases from 600 MPa at R=0.6 to 400 MPa at R=0.2, in agreement with the tendency for the fatigue strength of crystalline alloys.

Although the fatigue strength of Fe-Si-B amorphous wire in air with RH=65 % is lower than that of piano wire and high carbon steel wire, the reduction of humidity is expected to give rise to a remark-

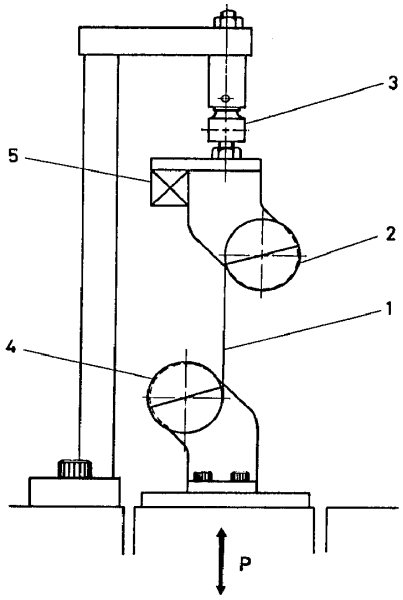


1. Specimen, 2. Upper capstan grip
3. Universal joint, 4. Lower capstan grip
5. Balance weight

Fig. 19 Schematic illustration of tensile-type fatigue testing machine.

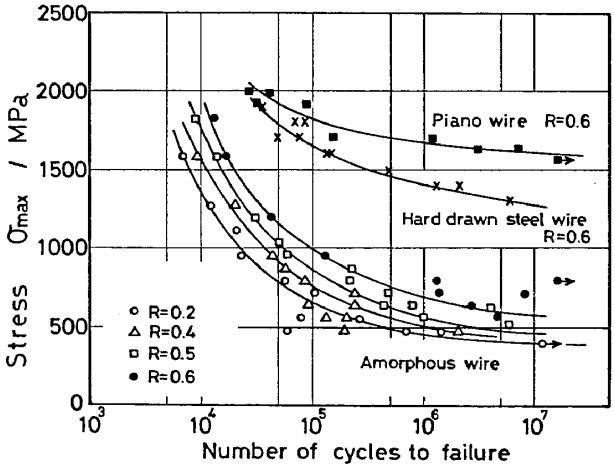


Fig. 20 Tensile fatigue curves for $Fe_{75}Si_{10}B_{15}$ amorphous wires at various stress ratios.

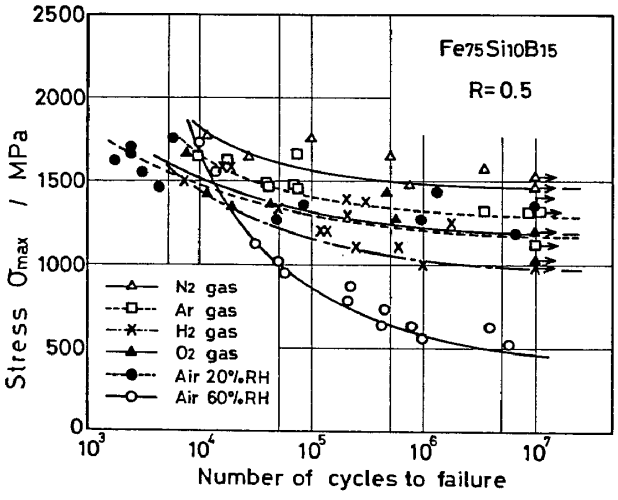


Fig. 21 Tensile fatigue curves for $Fe_{75}Si_{10}B_{15}$ amorphous wires in argon, nitrogen, oxygen, hydrogen or air atmosphere.

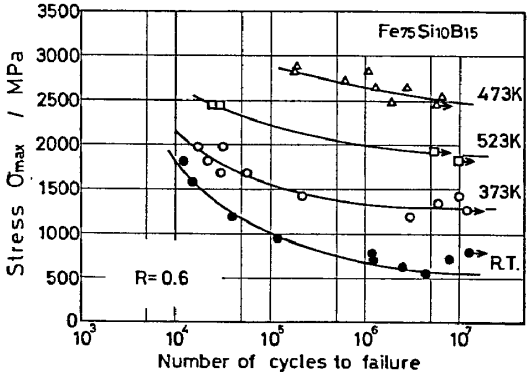


Fig. 22 Tensile fatigue curves for $Fe_{75}Si_{10}B_{15}$ amorphous wires at various temperatures.

able enhancement of fatigue strength of $Fe_{75}Si_{10}B_{15}$ amorphous wires at R=0.5 in air with RH=20 and 65 % as well as in nitrogen, argon, hydrogen and oxygen with RH=20 %. As shown in Fig. 21, the fatigue limit in air increases significantly from 500 MPa at RH=65 % to 1200 MPa at RH=20 %. Furthermore, in various kinds of gases with a constant RH (≃20 %) the fatigue limit exhibits nearly the same values. The fatigue limit depends strongly on the humidity in their gases but is independent of the kind of gases. It is thus concluded that the reduction of moisture enhances significantly the tensile type fatigue strength of Fe-Si-B amorphous wires, in agreemnt with the result under dynamic bending load.

3. Influence of testing temperature on fatigue strength

The rise of fatigue test temperature brings about the elimination of moisture in air and hence the fatigue strength is expected to be remarkably enhanced at elevated temperatures. It is also important to clarify the highest temperature at which high fatigue strength remains uchanged. Figure 22 shows the influence of testing temperature on the $\sigma_{max}$-$N_f$ curve of $Fe_{75}Si_{10}B_{15}$ amorphous wire in air. As the temperature rises from 373 to 473 K, the fatigue limit increases significantly from 1290 to 2500 MPa and then decreases to 1890 MPa with further rising testing temperature to 523 K. The enhanced fatigue strength at 473 K is probably because moisture in air is completely eliminated and the highly concentrated repetitive stress is easily released through an increase of the ease of atomic movement. On the other hand, the decrease of fatigue strength at 523 K is presumably due to a large decrease of flow stress of the amorphous alloy with rising temperature.

4. Fracture morphology

Figures 23 and 24 show the fracture surface appearance of $Fe_{75}Si_{10}B_{15}$ amorphous wires fractured under dynamic tensile load at different stress ratios, atmospheres and testing temperatures. The features of the fracture surface are smmarized as follows; (a) the surface can be divided into a fatigue failure region caused by repetitive tensile load and a subsequent rapidly failured region. (b) The fatigue failure initiates on the outside surface of the wire and propagates radiately to an inside region accompanied by an arc-like fracture pattern. (c) The region of crack initiation is flat and shows featureless appearance. One can remind that these features are

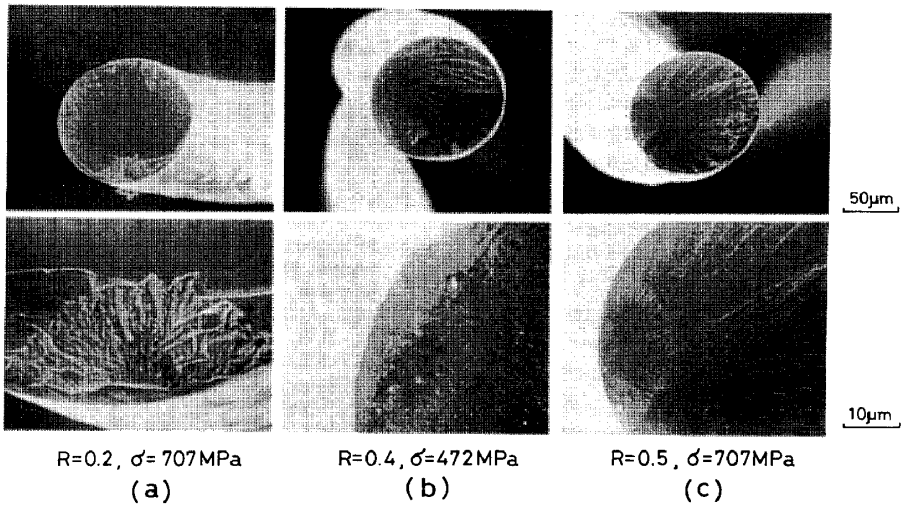


Fig. 23 Scanning electron micrographs of tensile fatigue fracture surface at various stress ratios.

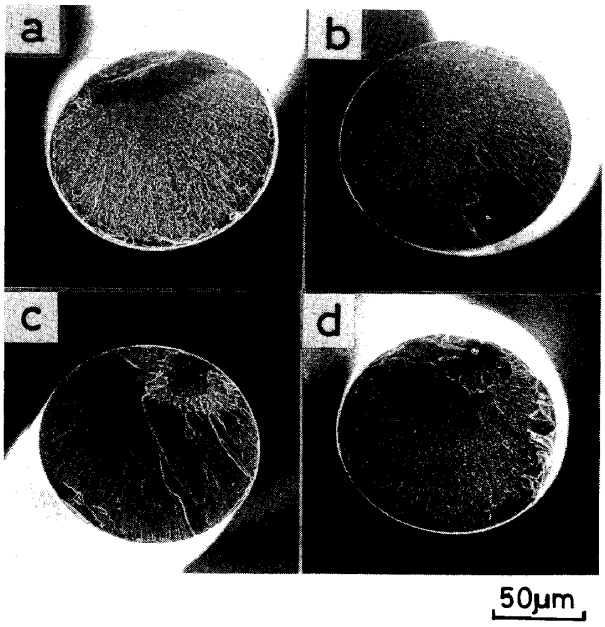


Fig. 24 Scanning electron micrographs of tensile fatigue fracture surfaces in (a) argon gas, (b) nitrogen gas, (c) air at 373 K and (d) air at 473 K.

just the same as those for the fracture surface under dynamic bending load shown in Fig. 10. As shown in Fig. 23, as the stress ratio decreases, the ruggedness in the fatigue failure region becomes coarse and the flat area near the crack initiation site becomes narrow. This change suggests that the propagation distance of fatigue crack in one repetition increases with decreasing stress ratio, i.e., with increasing stress amplitude, being consistent with the decrease in fatigue strength on the $\sigma_{max}$-$N_f$ curve shown in Fig. 20.

The feature of the fatigue fracture surface is independent of the difference in nitrogen, argon, oxygen, hydrogen and air as exemplified in Fig. 24 (a) and (b). No apprecable difference in fracture surface is seen at 273 and 373 K. However, the fracture surface at 473 K at which the highest fatigue strength was obtained exhibits a large reduction of the fatigue failure area, indicating that the initiation of fatigue crack was significantly suppressed.

Figure 25 shows the correlation between the ratio of fatigue failure area (A) to the entire fracture area ($A_o$) and the maximum applied stress ($\sigma_{max}$) for $Fe_{75}Si_{10}B_{15}$ amorphous wires. As the $\sigma_{max}$ increases, the ratio $A/A_o$ decreases and the fatigue failure area becomes narrower. The tendency is independent of the humidity in air and the difference in environmental gases. Thus, the propagation of fatigue crack is independent of atmosphere and the atmosphere gives a great influence on the intitiation stage of fatigue crack for the amorphous wire, i.e., the reduction in humidity supresses the initiation of fatigue crack, leading to high fatigue strength.

## VIII. Structural Change Cuased by Fatigue Deformation

It is very important to clarify the structural change in an amorphous wire caused by fatigue deformation. A previous X-ray diffraction study[44] on the amorphous structure in $Ni_{75}Si_8B_{17}$ and $Co_{72.5}Si_{12.5}B_{15}$ ribbon samples before and after fatigue deformation shows that a slightly detectable change takes place in the second diffraction peak. However, the problem whether this change is due to the transition of the amorphous structure into a more dense or random atomic configuration remains unsolved. The result suggests that the clarification of the fatigue-induced structural change by X-ray diffractometry is rather difficult. The difficulty seems to increase further for the amorphous wire subjected to fatigue deformation. Very recently, the change in $\Delta H_{relax}$ of Fe-Si-B and Fe-Cr-Si-B amorphous wires by fatigue deformation has been examined by differential scan-

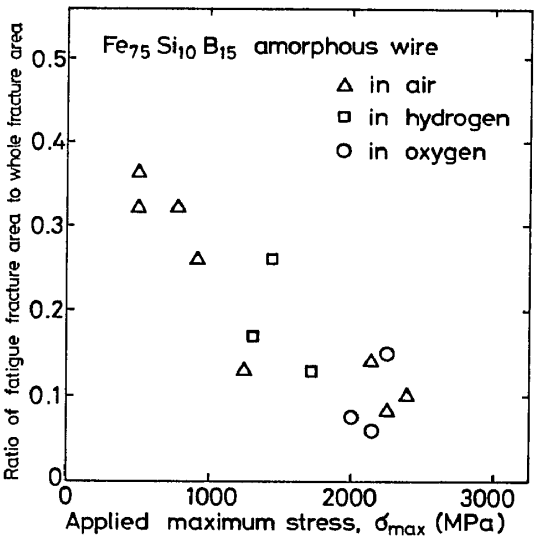


Fig. 25 Correlation between applied maximum stress and the ratio of fatigue fracture area to entire fracture area for $Fe_{75}Si_{10}B_{15}$ amorphous wires subjected to tensile fatigue failure at 293 K in various atmospheres.

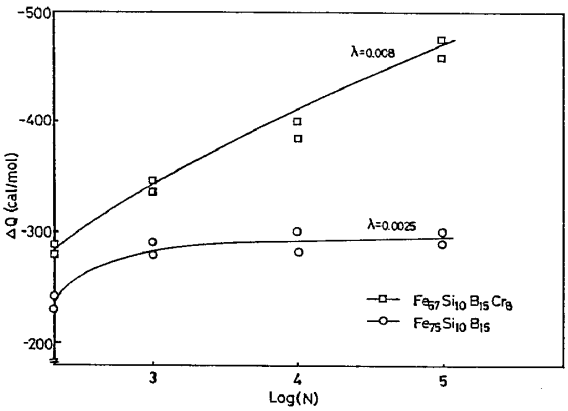


Fig. 26 Change in the relaxation enthalpy $\Delta H_{relax}$ of $Fe_{75}Si_{10}B_{15}$ and $Fe_{67}Cr_8Si_{10}B_{15}$ amorphous wires with number of cycles of bending strain.

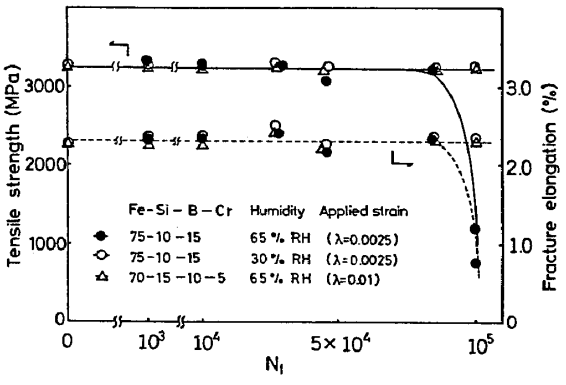


Fig. 27 Changes in the tensile fracture strength ($\sigma_f$) and fracture elongation ($\varepsilon_f$) of $Fe_{75}Si_{10}B_{15}$ and $Fe_{70}Cr_5Si_{15}B_{10}$ amorphous wires subjected to fatigue deformation at various numbers of cycles of bending strain.

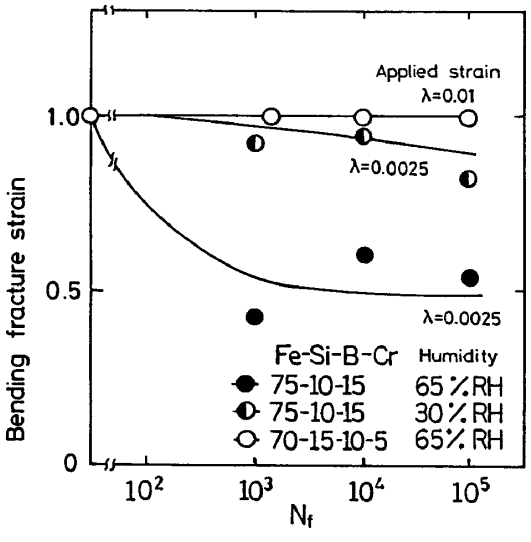


Fig. 28 Change in the bending fracture strain of $Fe_{75}Si_{10}B_{15}$ and $Fe_{70}Cr_5Si_{15}B_{10}$ amorphous wires subjected to fatigue deformation at various numbers of cycles of bending strain.

ning calorimetry (DSC). Figure 26 plots $\Delta H_{relax}$ values of $Fe_{75}Si_{10}B_{15}$ and $Fe_{67}Cr_8Si_{10}B_{15}$ amorphous wires as a function of the number of cycles under high repetitive bending strain of $\lambda$=0.0129 just below the fatigue limit in air with RH=65 %[45]. The $\Delta H_{relax}$ represents the relaxation enthalpy in the temperature range from room temperature to 723 K. $\Delta H_{relax}$ of the Fe-Si-B and Fe-Cr-Si-B wires is about 960 and 1190 J/mol, respectively, at $N_f$=0 and increases significantly with $N_f$=$10^5$. Furthermore, the onset temperature at which the structural relaxation begins to occur, $T_{relax}$, decreases from 441 K at $N_f$=0 to 399 K at $N_f$=$10^5$ for $Fe_{67}Cr_8Si_{10}B_{15}$ wire. The increase in $\Delta H_{relax}$ and the decrease in $T_{relax}$ suggest a possibility that the amorphous structure changed into a more disordered atomic configuration by fatigue deformation. This result is in marked contrast to the concept that fatigue deformation causes a temperature rise at a highly stress-concentrated site and hence the structural change into a more relaxed (dense) atomic configuration.

## IX. Mechanical Strength and Ductility of Amorphous Alloy Wires Subjected to Fatigue Deformation

The change in static mechanical properties by fatigue deformation is presented in this section. This problem is important from an engineering point of view as well as in an understanding of structural change caused by fatigue deformation. Figure 27 shows the changes in $\sigma_f$ and $\varepsilon_f$ of $Fe_{75}Si_{10}B_{15}$ and $Fe_{70}Cr_5Si_{10}B_{15}$ amorphous wires as a function of $N_f$[46]. No change in $\sigma_f$ is seen even at $N_f$=$10^5$ for the Fe-Cr-Si-B wire in air with RH=65 % and the Fe-Si-B wire in air with RH=30 %, while $\varepsilon_f$ tends to increase slightly in the vicinity of $N_f$=$3\times10^4$. This trend in $\sigma_f$ and $\varepsilon_f$ allows us to reconfirm that the fatigue deformation does not bring about a more relaxed structural change so as to accelerate thermal embrittlement, being consistent with the result obtained by DSC. Figure 27 also shows that $\sigma_f$ and $\varepsilon_f$ of the Fe-Si-B wires tested in air with RH=65 % decrease significantly at $N_f$=$10^5$. These decreases are probably because of fine cracks induced by fatigue deformation. Figure 28 shows the change in the fracture strain of the Fe-Si-B and Fe-Cr-Si-B amorphous wires in a bend test as a function of $N_f$. It is particularly notable that the Fe-Cr-Si-B wire with a high fatigue strength has good bend ductility similar to that of the as-quenched wire even after the severe fatigue deformation at $\lambda$=0.01 and $N_f$=$10^5$ and no detectable fatigue-induced embrittlement is seen.

## X. Possibility of Practical Use of Amorphous Alloy Wires as a Reinforcing Material in Rubber Tire

As described above, the iron-, cobalt- and nickel-based amorphous wires containing about 5 at% Cr exhibit very high fatigue strength at room temperature and elevated temperatures even in highly humid air, in addition to high static mechanical strength, good bend ductility and good corrosive resistance. Furthermore, their dynamic and static strengths and corrosion resistance are much larger than those of conventional piano wire and high carbon steel wire. In addition, the Fe-Cr-Si-B amorphous wires have a lower specific weight, a lower Young's modulus, a larger pseudoelasticity and a large capacity to absorb mechanical vibration. These unique advantages are attractive enough to start the fundamental research with the aim of using practically the Fe-Cr-Si-B amorphous wires as a reinforcing material in rubber tire, etc. Although there are some unsolved problems of the wetability of the wire to base material, expensive cost of the raw material due to the dissolution of boron and so forth, we believe that the amorphous wires would be practically used in near future as a new type of reinforcing materials in various kinds of base materials because of the excellent properties which cannot be obtained for the other metallic materials.

## XI. The Other Functional Properties and Current Applications of Amorphous Alloy Wires

Finally, it appears valuable to introduce some functional characteristics except mechanical properties for iron- and cobalt-based amorphous wires. As summarized in Table 4[47], the amorphous wires have some characteristics resulting from an amorphous structure and alloy compositions themselves; (a) good soft ferromagnetism of high saturated magnetization, low coercive force and high permeability, (b) a wide variation of magnetostrain ranging from zero to $30\times10^{-6}$-$40\times10^{-6}$, and (c) high electrical resistivity of 120 to 190 μΩcm. Additionally, it should be noticed that the amorphous wires exhibit simultaneously the other unique characteristics resulting from a fine wire form; (a) a geometrical isotropy over the entire cross section leading to a good flexibility, (b) good cold- and warm-drawability to 10 μm diameter without intermediate annealing, (c) a thermal exansion coefficient of $8.7\times10^{-6}$ $K^{-1}$ lower by about 30 % than that of piano wire, (d) huge Burkhausen jump due to a quick reversion of magnetiza-

Table 4 Various kinds of functional properties of Fe- and Co-based ferromagnetic amorphous wires.

| Properties resulting from a disordered structure and alloy compositions | Properties resulting from a fine wire form with a circular cross section |
|---|---|
| (a) Excellent soft ferromagnetism<br>Fe base:<br>High saturated magnetization($B_S$) 6kG<br>Low coercive force($H_C$) 0.2Oe<br>High permeability($\mu$) 7000 at 10kHz | (a) Geometrical isotropy over the entire cross section<br>Good flexibility which enables to twist, weave and knit. Easy formation of composite materials |
| (b) Wide variation of magnetostrain<br>Fe base:<br>High magnetostrain constant($\lambda_S$)<br>$30\times10^{-6}$ - $40\times10^{-6}$<br>Co base:<br>Low magnetostrain constant($\lambda_S$) $\simeq 0$ | (b) Good cold- and warm-drawability to $\simeq$10 $\mu$m diameter without intermediate annealing<br>Drawing causes an enhancement of mechanical strengths and elongation. |
| (c) High electrical resistivity<br>130 - 190 $\mu\Omega$cm | (c) Low thermal expansion coefficient |
| (d) High mechanical strength<br>High fatigue strength<br>High hardness<br>High ductility<br>High corrosion resistance | (d) Huge Burkhausen jump<br>Fe base:<br>Quick reversion of magnetization at an applied field equal to $H_C$. |
| | (e) Matteucci effect<br>Large output of sharp voltage pulse corresponding to the alternation of magnetic field |

tion at an applied field equal to coercive force, (e) matteucci effect leading to the large output of sharp voltage pulse corresponding to the alternation of magnetic field. Owing to these unique functional properties as well as good mechanical properties, the iron- and cobalt-based amorphous wires have already been used practically as sensing elements in magneto-electronic devices which demand these magnetic, electrical and mechanical properties as well as the fine geometry. If the amorphous wires are practically used as a reinforcing material such as the cord wire in rubber tire, the amorphous alloy wires are expected to occupy an indisputable position as a new type of engineering materials.

## References

(1) T. Masumoto and R. Maddin, Acta Met., 19 (1971), 725.
(2) H.L. Leamy, H.S. Chen and T.T. Wang, Met. Trans., 3A (1972), 699.
(3) T. Masumoto, I. Ohnaka, A. Inoue and M. Hagiwara, Scripta Met., 15 (1981), 293.

(4) M. Hagiwara, A. Inoue and T. Masumoto, Met. Trans., 13A (1982), 373.

(5) A. Inoue, M. Hagiwara and T. Masumoto, J. Mater. Sci., 17 (1982), 580.

(6) M. Hagiwara, A. Inoue and T. Masumoto, Mater. Sci. Eng., 54 (1982), 197.

(7) M. Hagiwara, A. Inoue and T. Masumoto, Proc. 5th Int. Conf. on Rapidly Quenched Metals, North-Holland, Amsterdam (1985) p.1779.

(8) H.S. Chen, R.C. Sherwood, S. Jin, G.C. Chi, A. Inoue, T. Masumoto and M. Hagiwara, J. Appl. Phys., 56 (1984), 1796.

(9) K. Mohri, J. Yamasaki and T. Kondo, Proc. 5th Int. Conf. on Rapidly Quenched Metals, North-Holland, Amsterdam (1985) p.1659.

(10) H. Matsuki and K. Murakami, IEEE Trans. Magnetics, MAG-21 (1985), 1738.

(11) A. Inoue, N. Yano, H.S. Chen, M. Hagiwara and T. Masumoto, Mater. Sci. Eng., 77 (1986), 45.

(12) M. Hagiwara and S. Ide, private communication, Unitika Ltd., Uji 611, Japan.

(13) A. Inoue, S. Furukawa, M. Hagiwara and T. Masumoto, Met. Trans., 18A (1987), 621.

(14) J.C. Hubert, F. Molland and B. Lux, Z. Metallk., 64 (1973), 835.

(15) I.G. Butler, W. Jurz and B. Lux, Fibre Sci. Tech., 5 (1972), 243.

(16) D.J. Thorne, Fibre Sci. Tech., 7 (1974), 79.

(17) R.B. Pond and R. Maddin, Trans. Met. Soc. AIME, 245 (1969), 2475.

(18) C.E. Mobley, A.H. Clauer and B.A. Wilcox, J. Inst. Metals, 100 (1972), 142.

(19) R.B. Pond and J.M. Winter,Jr., Mater. Sci. Eng., 23 (1976), 71.

(20) R.E. Maringer and J. Schneider, Phys. Status Solidi (a), 26 (1974), 71.

(21) G.E. Taylor, Phys. Rev., 23 (1924), 655.

(22) I. Ohnaka, T. Fukusako and T. Daido, J. Japan Inst. Metals, 45 (1981), 751.

(23) H. Wiesner and J. Schneider, Phys. Stat. Sol. (a), 26 (1974), 21.

(24) T. Goto, M. Nagano and N. Vehara, Trans. Japan Inst. Metals, 18 (1977), 759.

(25) T. Masumoto, A. Inoue, M. Hagiwara, I. Ohnaka and T. Fukusako, Proc. 4th Int. Conf. on Rapidly Quenched Metals, ed. T. Masumoto and K. Suzuki, Japan Inst. Metals, Sendai (1981) p.47.

(26) A. Inoue, T. Masumoto, N. Yano, A. Kawashima, K. Hashimoto and

T. Masumoto, J. Mater. Sci., 20 (1985), 97.
(27) A. Inoue, N. Yano and T. Masumoto, J. Mater. Sci., 19 (1984), 3786.
(28) M. Hagiwara, A. Inoue and T. Masumoto, Sci. Rep. Res. Inst. Tohoku Univ., 29A (1981), 351.
(29) M. Hagiwara, A. Inoue and T. Masumoto, Met. Trans., 12A (1981), 1027.
(30) A. Inoue, H.S. Chen, J.T. Krause, T. Masumoto and M. Hagiwara, J. Mater. Sci., 18 (1983), 2743.
(31) H.S. Chen, J.T. Krause and E. Coleman, J. Non-Cryst. Solids, 78 (1975), 157.
(32) S.S. Brenner, J. Appl. Phys., 27 (1956), 1484.
(33) H. Sunada, H. Izumi, Y. Hayashi and T. Masumoto, J. Japan Inst. Metals, 50 (1986), 624.
(34) M. Hagiwara, A. Inoue and T. Masumoto, unpublished research (1984).
(35) A. Inoue, H.S. Chen, J.T. Krause and T. Masumoto, J. Non-Cryst. Solids, 61&62 (1984), 949.
(36) H.S. Chen, J. Appl. Phys., 49 (1978), 3289.
(37) H.S. Chen, J. T. Krause, A. Inoue and T. masumoto, Scripta Met., 17 (1983), 1413.
(38) A. Inoue, T. Masumoto, M. Hagiwara and H.S. Chen, Scripta Met., 17 (1983), 1205.
(39) F.E. Luborsky, H.H. Liebermann and J.L. Walter, Proc. of the Conf. on Metallic Glasses, eds. C. Hargitai, I. Bakonyi and T. Kemeny, Central Res. Inst. for Physics, Budapest (1980) vol.I, p.203.
(40) S. Kavesh, Metallic Glasses, ASM, Ohio (1978), p.36.
(41) J. Ishihara, private communication(1982), Hitachi Research Laboratory, Hitachi Ltd., Hitachi 319-12.
(42) M. Hagiwara, A. Inoue and T. Masumoto, unpublished research (1984).
(43) M. Doi, K. Sugiyama, T. Tono and T. Imura, Proc. 4th Int. Conf. on Rapidly Quenched Metals, ed. T. Masumoto and K. Suzuki, Japan Inst. Metals, Sendai (1981) p.1349.
(44) H. Izumi, H. Sunada, Y. Hayashi and T. Masumoto, J. Japan Inst. Metals, 48 (1984), 371.
(45) A. Menju, M. Hagiwara, A. Inoue and T. Masumoto, unpublished research.
(46) M. Hagiwara, A. Menju, A. Inoue and T. Masumoto, unpublished research.
(47) Unitika Commercial Catalog (1984).